Int. J. Fuzzy Syst. (2023) 25(4):1674–1688
https://doi.org/10.1007/s40815-023-01469-2

Robust H-infinity Fuzzy Output Feedback Control for Path Following of FWID-EVs with Actuator Saturation

Taiyou Liu[1] · Xiaowei Wang[1] · Jing Zhao[1,2] · Pak Kin Wong[3] · Yongfu Wang[1]

Received: 19 July 2022 / Revised: 9 November 2022 / Accepted: 16 January 2023 / Published online: 2 March 2023

Abstract This article introduces a robust H-infinity fuzzy static output feedback (RHF-SOF) control with norm-bounded strategy to enhance the path-following performance for the four-wheel-independent-driven electric vehicles (FWID-EVs). Firstly, taking the parameter uncertainties including vehicle mass, moment of inertia, longitudinal velocity, and tire cornering stiffness into account, a fuzzy optimization model is constructed to approximate the nonlinear characteristic of the vehicle system using both the parameter uncertainty reduction strategy and polytope reduction strategy. Secondly, with consideration of the difficulty of the online lateral velocity measurement, a Lyapunov stability-based RHF-SOF control with the gain scheduling method is proposed to control the variables of the path following. Thirdly, since the actuator saturation can deteriorate the control performances, a norm-bounded strategy is designed to address the nonlinear saturation problem. The proposed controller is verified and evaluated through the hardware-in-the-loop experimental test with different maneuvers.

Keywords Path following · H infinity · Fuzzy · Output feedback control · Actuator saturation

Nomenclature

m	Mass of vehicle
$m_{\max}/m_{\min}$	Maximum/minimum value of mass
I_z	Moment of inertia
$I_{z\max}/I_{z\min}$	Maximum/minimum value of moment of inertia
CG	Center of gravity
C_f/C_r	Front/rear cornering stiffness
$C_{f\max}/C_{f\min}$	Maximum/minimum front cornering stiffness
$C_{r\max}/C_{r\min}$	Maximum/minimum rear cornering stiffness
l_f/l_r	Distance between CG to front/rear axle
F_{yf}/F_{yr}	Front/rear lateral forces
v_x/v_y	Longitudinal/lateral velocity of vehicle
r	Yaw rate of vehicle
M_z	External yaw moment
α_f/α_r	Slip angles of front/rear wheel
ψ_d/ψ_h	Desired/actual heading angle
ψ	Heading error
e	Lateral offset
ρ	Curvature of the desired path
δ	Front wheel steering angle
L_{ij}	Distance between the vertex coordinates
$sat(u)$	Saturation function of actuator input

✉ Jing Zhao
zhaoj@mail.neu.edu.cn

Taiyou Liu
2010116@stu.neu.edu.cn

Xiaowei Wang
2210119@stu.neu.edu.cn

Pak Kin Wong
fstpkw@um.edu.mo

Yongfu Wang
yfwang@mail.neu.edu.cn

[1] School of Mechanical Engineering and Automation, Northeastern University, Shenyang 110819, Liaoning, China

[2] State Key Laboratory of Synthetical Automation for Process Industries, Northeastern University, Shenyang 110819, Liaoning, China

[3] Department of Electromechanical Engineering, University of Macau, Taipa 999078, Macau

1 Introduction

Under the dual crisis of serious environmental pollution and oil resource shortage, many auto manufacturers have dedicated to the development of the electric vehicles (EVs) to reduce vehicle exhaust emissions and fuel consumption [1, 2]. For the purposes of stability and safety of the EVs, the electric vehicle control system needs to be further studied. Due to its unique dynamic system and drive system, the FWID-EVs have independent controllable torque of each drive wheel compared with the ordinary EVs, which brings enormous advantages to the vehicle control system [3]. In addition, the path-following performance is a crucial factor of the FWID-EV control systems that concern with vehicle active safety and did draw much attention in automotive technology research in recent years [4–6]. Consequently, this research intends to study the FWID-EVs to enhance the vehicle path-following performance.

Regarding the practical application of control system of the EVs, the vehicle parameters are uncertain, such as the vehicle mass, moment of inertia, and tire cornering stiffness [7–9]. A T–S fuzzy-based sliding mode control approach was adopted to address the parameter uncertainty problem of tire cornering stiffness and ensure control performance [10]. These uncertain parameters will impact the analysis of the vehicle lateral dynamics and controller performance. The observer-based fuzzy controller for EVs was constructed with the uncertainties of vehicle mass and moment of inertia in consideration [11]. By means of the IT-2 fuzzy method, Ren et al. discussed the lateral stability control issue for EVs with actuator saturation and sensor failures [12]. To address the path-following problem in autonomous ground vehicles, a linear fractional transformation (LFT)-based H_∞ SOF controller was developed [13].

Even though the above research can properly handle the parameters problem, the velocity is regarded as fixed in most studies, which does not correspond to the actual situation. And the gain scheduling control strategy that utilizes polytope to deal with the varying velocity is regarded as an effective method [14, 15]. Therefore, this paper intends to combine the LFT strategy and the gain scheduling control strategy to deal with the EVs' uncertainty problem with varying speed.

In the existing investigations, vehicle state information is usually used for constructing the feedback loop of the control system. For FWID-EVs, accurate vehicle state measurements are required for the path-following control [16, 17]. And the lateral velocity is closely associated with the vehicle motion state. Because of the complex working environment, it is difficult to guarantee the precise measurement of the lateral velocity [18]. Zhang *et al*. transformed the output to state feedback problem and proposed an observer-based output feedback control method for a class of interconnected systems [19]. Chang et al. discussed the output feedback stabilization problem for a class of cascade nonlinear ODE-PDE systems [20].

However, the LMI variables constructed by the above methods tend to have more structural constraints that do not provide more degrees of freedom to solve the inequality. Recent research indicates that the Robust H-infinity output feedback method can properly manage uncertain system models and noise characteristics, and effectively reduce the structural constraints on LMI variables and improve the degree of freedom of LMI solutions [21–24]. Zhao et al. proposed an H-infinity SOF controller based on multi-objective frequency domain to obtain unmeasured active suspension systems status information, thereby improving the stability of the suspension [25]. Since the conceptual simplicity, ease of implementation of the H-infinity output feedback method, the robust H-infinity fuzzy static output feedback (RHF-SOF) control strategy which can online obtain the state information of the lateral velocity is investigated in this work.

With the measured state variables, the control variables of the control strategy can be confirmed. Then, the output variables are generated and transmitted to the actuator. The desired control effect will be attenuated when the actuator is saturated, because of the certain physical limitation of the actuator [26, 27]. In [28], an active vibration control approach was presented to handle the actuator saturation of the seismic excited building. For nonlinear 3-DOF helicopters, the distributed cooperative control with actuator saturation and faults was investigated in [29]. Moreover, the synchronous optimal control problem for the actuator saturation of nonlinear systems was discussed in [30]. So far, the research on the actuator saturation of FWID-EVs is rather limited.

Hence, the actuator saturation is still a challenging issue for the path-following control design of nonlinear FWID-EVs.

Inspired by all the problems mentioned above, this research describes the RHF-SOF path-following control strategy, and the actuator saturation of the nonlinear FWID-EVs are considered. The innovative points of this work can be summarized as follows:

(1) An RHF-SOF control approach is developed for nonlinear FWID-EVs with consideration of parameter uncertainties, nonlinear characteristics, and actuator saturations;
(2) A fuzzy optimization model is developed by combining the LFT strategy and the gain scheduling control strategy to handle the nonlinearities of the parameters;
(3) A norm-bounded strategy is designed to guarantee the stability of the controller in the presence of actuator saturation.

The rest research is organized as follows. The system modeling is covered in Section 2. The main results of the RHF-SOF are explained in Section 3. In Section 4,

experimental results are discussed. Finally, Section 5 presents the conclusion.

2 Problem formulation

2.1 Description of Vehicle Lateral Behavioral Model

In this work, lateral dynamics is taken into account and the typical vehicle lateral behavioral model is shown in Fig. 1. The lateral behavioral model can be derived as [31] follows:

$$\begin{cases} \dot{v}_y = F_{yf}/m + F_{yr}/m - v_x r + d_1 \\ I_z \dot{r} = M_z + l_f F_{yf} - l_r F_{yr} + d_2 \\ \dot{\psi} = \dot{\psi}_h - \dot{\psi}_d = r - \rho v_x \\ \dot{e} = v_y + v_x \psi + d_3 \end{cases} \tag{1}$$

Among them, m, v_x, v_y, I_z, F_{yf}, F_{yr}, r, M_z and e are unknown parameters that change over time. All unknown parameters are explained in Nomenclature. Choose $x(t) = [v_y \quad r \quad \psi \quad e]^T$ as the state variable. Then, motivated by the above discussions, the dynamic description of the vehicle model is described as follows:

$$\dot{x}(t) = Ax(t) + B_1\omega(t) + B_2u(t)\,, \tag{2}$$

where $\omega(t) = [d_1 \quad d_2 \quad \rho \quad d_3]^T$, $u(t) = [\delta \quad \Delta M_z]^T$, and

$$A_i = \begin{bmatrix} -\frac{C_f + C_r}{mv_x} & -\frac{l_f C_f - l_r C_r}{mv_x} - v_x & 0 & 0 \\ -\frac{l_f C_f - l_r C_r}{I_z v_x} & -\frac{l_f^2 C_f + l_r^2 C_r}{I_z v_x} & 0 & 0 \\ 0 & 1 & 0 & 0 \\ 1 & 0 & v_x & 0 \end{bmatrix},$$

$$B_1 = \begin{bmatrix} 1 & 0 & 0 & 0 \\ 0 & 1 & 0 & 0 \\ 0 & 0 & v_x & 0 \\ 0 & 0 & 0 & 1 \end{bmatrix}, B_2 = \begin{bmatrix} \frac{C_f}{m} & 0 \\ \frac{l_f C_f}{I_z} & \frac{1}{I_z} \\ 0 & 0 \\ 0 & 0 \end{bmatrix}$$

2.2 Fuzzy Model of FWID-EV

As shown in Fig. 2, the parameter uncertainty of the vehicle longitudinal velocity is represented by a triangular polytope [32]. Time-varying parameters v_x and $1/v_x$ are bounded in $[v_{x\min} \; v_{x\max}]$ and $[1/v_{x\max} \; 1/v_{x\min}]$. In triangular polytope, it covers all the possible choices for the parameter pair $[v_x \; 1/v_x]$. The vertex coordinates are expressed as $\Lambda_i = (\varphi_{xi}, \varphi_{yi}), (i = 1, 2, 3)$. The intersection of the tangents of the velocity curve at points Λ_1, Λ_2 , and Λ_3.

The coordinates of Λ_i can be given as follows:

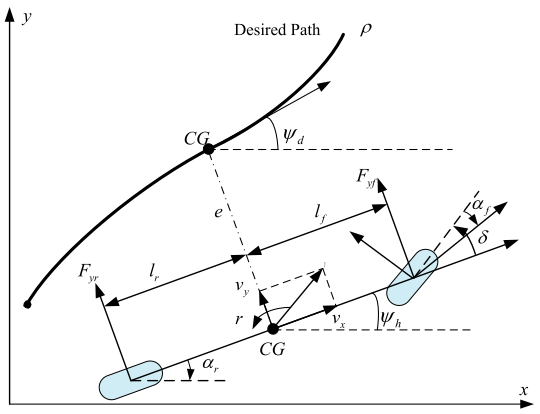

Fig. 1 Vehicle lateral behavioral model

$$\varphi_{x1} = v_{x\min}, \varphi_{x2} = v_{x\max}, \varphi_{x3} = \frac{2v_{x\max}v_{x\min}}{v_{x\min} + v_{x\max}}$$
$$\varphi_{y1} = \frac{1}{v_{x\min}}, \varphi_{y2} = \frac{1}{v_{x\max}}, \varphi_{y3} = \frac{2}{v_{x\min} + v_{x\max}}.$$

The sum of the vertex coordinates is utilized to represent the premise vector v_x and $1/v_x$ by

$$v_x = \sum_{i=1}^{3} \alpha_i(t)\varphi_{xi}, \frac{1}{v_x} = \sum_{i=1}^{3} \alpha_i(t)\varphi_{yi}\,, \tag{3}$$

where the weighting functions $\alpha_i(t)$ are chosen as

$$\alpha_1 = \frac{L_{34}}{L_{35}}\frac{L_{25}}{L_{12}}, \alpha_2 = \frac{L_{34}}{L_{35}}\frac{L_{15}}{L_{12}}, \alpha_3 = \frac{L_{45}}{L_{35}}$$

with L_{ij} representing the distance between the points Λ_i and Λ_j. For $i = 1, 2, 3$, Eq. (3) meets $\alpha_i(t) > 0$, $\sum_{i=1}^{3} \alpha_i(t) = 1$, and the vehicle model is characterized as

$$\dot{x}(t) = \sum_{i=1}^{3} \alpha_i(t)[A_i x(t) + B_{1i}\omega(t) + B_2 u(t)]\,, \tag{4}$$

where

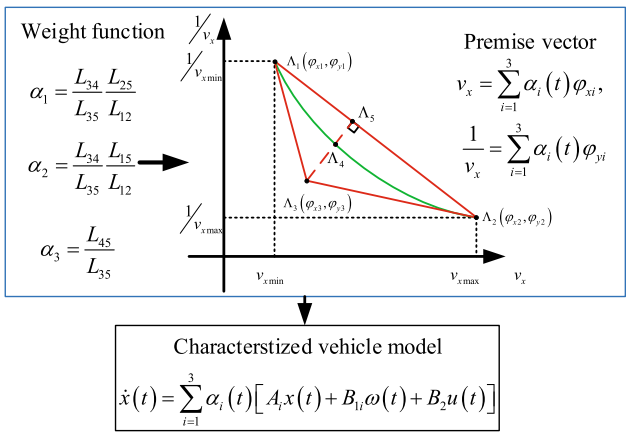

Fig. 2 Triangular polytope of the longitudinal velocity parameter

$$A_i=\begin{bmatrix} -\frac{\varphi_{yi}(C_J+C_r)}{m} & -\frac{\varphi_{yi}(l_fC_J-l_rC_r)}{m}-\varphi_{xi} & 0 & 0 \\ -\frac{\varphi_{vi}(l_fC_I-l_rC_r)}{I_z} & -\frac{\varphi_{yi}\left(l_f^2C_J+l_r^2C_r\right)}{I_z} & 0 & 0 \\ 0 & 1 & 0 & 0 \\ 1 & 0 & \varphi_{xi} & 0 \end{bmatrix},$$

$$B_{1i}=\begin{bmatrix} 1 & 0 & 0 & 0 \\ 0 & 1 & 0 & 0 \\ 0 & 0 & -\varphi_{xi} & 0 \\ 0 & 0 & 0 & 1 \end{bmatrix},$$

Considering the variation of the driving condition, the parameters of the tire cornering stiffness are unknown and need to be considered in the concerned system. Therefore, it is defined that

$$\begin{cases} C_f = C_{f0}+\lambda_f \Delta C_f \\ C_r = C_{r0}+\lambda_r \Delta C_r \end{cases} \tag{5}$$

where the time-varying parameters λ_f and λ_r meet $|\lambda_i|\le 1,(i=f,r)$, and

$$C_{f0}=\frac{\left(C_{f\max}+C_{f\min}\right)}{2}, \Delta C_f=\frac{\left(C_{f\max}-C_{f\min}\right)}{2},$$
$$C_{r0}=\frac{(C_{r\max}+C_{r\min})}{2}, \Delta C_r=\frac{(C_{r\max}-C_{r\min})}{2}.$$

In addition, vehicle mass m and moment of inertia I_z also change since the payload variation. Then, $1/m$ and $1/I_z$ can be represented as follows:

$$\frac{1}{m}=\frac{1}{m_0}+\lambda_m\frac{1}{\Delta m}, \frac{1}{I_z}=\frac{1}{I_{z0}}+\lambda_{I_z}\frac{1}{\Delta I_z}, \tag{6}$$

where λ_m and λ_{I_z} are time-varying parameters that meeting $|\lambda_i|\le 1,(i=m,I_z)$, and

$$\frac{1}{m_0}=\frac{\left(\frac{1}{m_{\max}}+\frac{1}{m_{\min}}\right)}{2}, \frac{1}{\Delta m}=\frac{\left(\frac{1}{m_{\min}}-\frac{1}{m_{\max}}\right)}{2},$$
$$\frac{1}{I_{z0}}=\frac{\left(\frac{1}{I_{z\max}}+\frac{1}{I_{z\min}}\right)}{2}, \frac{1}{\Delta I_z}=\frac{\left(\frac{1}{I_{z\min}}-\frac{1}{I_{z\max}}\right)}{2}.$$

Furthermore, the varying C_f/m, C_r/m, C_f/I_z , and C_r/I_z can be constructed by

$$\frac{C_f}{m}=\frac{C_{f0}}{m_0}+\frac{\lambda_m C_{f0}}{\Delta m}+\frac{\lambda_f \Delta C_f}{m_0}+\frac{\lambda_f\lambda_m\Delta C_f}{\Delta m}$$
$$=\frac{C_{f0}}{m_0}+\lambda_1\vartheta_1,$$

$$\frac{C_r}{m}=\frac{C_{r0}}{m_0}+\frac{\lambda_m C_{r0}}{\Delta m}+\frac{\lambda_r\Delta C_r}{m_0}+\frac{\lambda_r\lambda_m\Delta C_r}{\Delta m}$$
$$=\frac{C_{r0}}{m_0}+\lambda_2\vartheta_2$$
$$\frac{C_f}{I_z}=\frac{C_{f0}}{I_{z0}}+\frac{\lambda_I C_{f0}}{\Delta I_z}+\frac{\lambda_f\Delta C_f}{I_{z0}}+\frac{\lambda_f\lambda_{I_z}\Delta C_f}{\Delta I_z},$$
$$=\frac{C_{f0}}{I_{z0}}+\lambda_3\vartheta_3$$
$$\frac{C_r}{I_z}=\frac{C_{r0}}{I_{z0}}+\frac{\lambda_m C_{r0}}{\Delta I_z}+\frac{\lambda_r\Delta C_r}{I_{z0}}+\frac{\lambda_r\lambda_{I_z}\Delta C_r}{\Delta I_z}$$
$$=\frac{C_{r0}}{I_{z0}}+\lambda_4\vartheta_4$$

where the unknown parameters $|\lambda_i|<1,(i=1,2,3,4)$, and

$$\vartheta_1=\frac{C_{f0}}{\Delta m}+\frac{\Delta C_f}{m_0}+\frac{\Delta C_f}{\Delta m},$$
$$\vartheta_2=\frac{C_{r0}}{\Delta m}+\frac{\Delta C_r}{m_0}+\frac{\Delta C_r}{\Delta m},$$
$$\vartheta_3=\frac{C_{f0}}{\Delta I_z}+\frac{\Delta C_f}{I_{z0}}+\frac{\Delta C_f}{\Delta I_z},$$
$$\vartheta_4=\frac{C_{r0}}{\Delta I_z}+\frac{\Delta C_r}{I_{z0}}+\frac{\Delta C_r}{\Delta I_z}$$

Without loss of universality, $\lambda_1=\lambda_2=\lambda_3=\lambda_4$ can be set, and the coefficient matrix can be written as $A_i=A_{0i}+\Delta A_i$, $B_2=B_{20}+\Delta B_2$, and

$$A_{0i}=\begin{bmatrix} -\frac{\varphi_{yi}(C_{f0}+C_{r0})}{m_0} & -\frac{\varphi_{yi}(l_fC_{f0}-l_rC_{r0})}{m_0}-\varphi_{xi} & 0 & 0 \\ frac\varphi_{yi}(l_fC_{f0}-l_fC_{r0})I_{z0} & -\frac{\varphi_{yi}\left(l_f^2C_{f0}+l_r^2C_{r0}\right)}{I_{z0}} & 0 & 0 \\ 0 & 1 & 0 & 0 \\ 1 & 0 & \varphi_{xi} & 0 \end{bmatrix},$$

$$\Delta A_i=\begin{bmatrix} -\varphi_{yi}(\lambda_1\vartheta_1+\lambda_2\vartheta_2) & -\varphi_{yi}(l_f\lambda_1\vartheta_1-l_r\lambda_2\vartheta_2) & 0 & 0 \\ varphi_{yi}(l_f\lambda_3\vartheta_3-l_r\lambda_4\vartheta_4) & -\varphi_{yi}\left(l_f^2\lambda_3\vartheta_3+l_r^2\lambda_4\vartheta_4\right) & 0 & 0 \\ 0 & 0 & 0 & 0 \\ 0 & 0 & 0 & 0 \end{bmatrix},$$

$$B_{20}=\begin{bmatrix} \frac{C_{f0}}{m_0} & 0 \\ \frac{l_fC_{f0}}{I_{z0}} & \frac{1}{I_{z0}} \\ 0 & 0 \\ 0 & 0 \end{bmatrix}, \Delta B_2=\begin{bmatrix} \lambda_1\vartheta_1 & 0 \\ l_f\lambda_3\vartheta_3 & \frac{\lambda_{I_z}}{\Delta I_z} \\ 0 & 0 \\ 0 & 0 \end{bmatrix}$$

The vehicle model can therefore be expressed as follows:

$$\dot{x}(t)=\sum_{i=1}^{3}\alpha_i(t)\cdot[(A_i+\Delta A_i)x(t)+B_{1i}\omega(t) +(B_{20}+\Delta B_2)u(t)], \tag{7}$$

where ΔA_i and ΔB_i represent the uncertainty caused by ΔC_f, ΔC_r, Δm , and ΔI_z, which can be formatted as

$$[\Delta A_i \quad \Delta B_2] = [H\Gamma E_{ai} \quad H\Gamma E_b], \tag{8}$$

where

$$E_{ai} = \begin{bmatrix} -\varphi_{yi}(\vartheta_1+\vartheta_2) & -\varphi_{yi}(l_f\vartheta_1 - l_r\vartheta_2) & 0 & 0 \\ -\varphi_{yi}(l_f\vartheta_3 - l_r\vartheta_4) & -\varphi_{yi}(l_f{}^2\vartheta_3 + l_r{}^2\vartheta_4) & 0 & 0 \\ 0 & 0 & 0 & 0 \end{bmatrix},$$

$$H = \begin{bmatrix} 1 & 0 & 0 \\ 0 & 1 & 1 \\ 0 & 0 & 0 \\ 0 & 0 & 0 \end{bmatrix}, \Gamma = \mathrm{diag}\{\lambda_1, \lambda_1, \lambda_{I_z}\}, E_b = \begin{bmatrix} \vartheta_f & 0 \\ l_f\vartheta_3 & 0 \\ 0 & \frac{1}{\Delta I_z} \end{bmatrix}.$$

The actuator input should be bounded in the controller design process due to the physical limits of the actuation system. Inspired by Du et al. [33], the saturation function $\mathrm{sat}(u)$ meets

$$\mathrm{sat}(u) = \begin{cases} -u_{\lim}, & u(t) \in (-\infty, -u_{\lim}) \\ u(t), & u(t) \in (-u_{\lim}, u_{\lim}) \\ u_{\lim}, & u(t) \in (u_{\lim}, +\infty) \end{cases}, \tag{9}$$

where $u_{\lim} > 0$ is the actuator input limitation.

Taking into account the nonlinearity of the system and the saturation function, the closed-loop system can be derived as follows:

$$\begin{aligned} \dot{x}(t) &= \sum_{i=1}^{3} \alpha_i(t)[(A_i + \Delta A_i)x(t) + B_{1i}\omega(t) \\ &\quad + (B_{20} + \Delta B_2)\bar{u}(t)] \\ &= \sum_{i=1}^{3} \alpha_i(t)[(A_i + \Delta A_i)x(t) + B_{1i}\omega(t) \\ &\quad + (B_{20} + \Delta B_2)\frac{1+\varepsilon}{2}u(t) \\ &\quad + (B_{20} + \Delta B_2)\left(\bar{u}(t) - \frac{1+\varepsilon}{2}u(t)\right)\Big] \end{aligned}, \tag{10}$$

where $\mathrm{sat}(u) = \bar{u}(t), 0 < \varepsilon < 1$.

2.3 Fuzzy SOF Controller

Regarding the vehicle system model's state variable, it is a remarkable fact that the lateral velocity v_y is hard to available online. Hence, the measured output is expressed as

$$y(t) = [r \quad \psi \quad e] = C_y x(t), \tag{11}$$

where

$$C_y = \begin{bmatrix} 0 & 1 & 0 & 0 \\ 0 & 0 & 1 & 0 \\ 0 & 0 & 0 & 1 \end{bmatrix}.$$

The SOF controller can then be acquired as follows:

$$\begin{aligned} u(t) &= \sum_{j=1}^{3} \alpha_j(t) K_j y(t) \\ &= \sum_{j=1}^{3} \alpha_j(t) K_j C_y x(t) \\ &= K_{sof} C_y x(t) \end{aligned}, \tag{12}$$

where $K_{sof} = \sum_{j=1}^{3} \alpha_j(t) K_j$ and K_j are the SOF controller gains to be designed.

The purpose of this work is to offer a RHF-SOF control strategy for the concerned vehicle dynamic system. Meanwhile, in the linear matrix inequalities control frame, the vehicle system in Eq. (10) is asymptotically stable and H_∞ performance is satisfied, namely

$$\gamma^2 \int_0^\infty \omega^T(t)\omega(t)\mathrm{d}t \geq \int_0^\infty z^T(t)z(t)\mathrm{d}t, \tag{13}$$

where γ represents the attenuation level of the concerned vehicle system.

Remark 1 The main challenge of this paper is devoted to propose a reasonable approach to solve the problem of numerous parameter uncertainties in vehicle systems and to design a controller based on the norm-bounded strategy to deal with the actuator saturation problem.

3 Main Result

In this section, the RHF-SOF control strategy for concerned vehicle dynamic systems with uncertain parameters and input saturation is adopted to enhance the path-following performance, and following lemmas are given to prove the main theorem.

Lemma 1 [34] *For the saturation function* $\mathrm{sat}(u)$, $\left\|\frac{1-\varepsilon}{2}u(t)\right\| \geq \left\|\bar{u}(t) - \frac{1+\varepsilon}{2}u(t)\right\|$ *holds for all input constraints satisfying* $|u(t)| \leq \frac{u_{lim}}{\varepsilon}$, *if and only if the following inequalities are true*:

$$\begin{aligned} &\left(\frac{1-\varepsilon}{2}\right)^2 u^{\mathrm{T}}(t)u(t) \\ &\quad \geq \left[\bar{u}(t) - \frac{1+\varepsilon}{2}u(t)\right]^{\mathrm{T}}\left[\bar{u}(t) - \frac{1+\varepsilon}{2}u(t)\right] \end{aligned} \tag{14}$$

Lemma 2 [33] *Given real matrices R and S with suitable dimensions, for all matrices F if* $\|F\| \le I$ *holds, then exists a prescribed scalar* $\xi > 0$ *such that*

$$RFS + S^{\mathrm{T}}F^{\mathrm{T}}R^{\mathrm{T}} \le \xi^{-1}RR^{\mathrm{T}} + \xi S^{\mathrm{T}}S \tag{15}$$

3.1 Stability Analysis and Controller Design

Theorem 1 *The concerned vehicle system in Eq. (10) is asymptotically stable and meets the desired performance in Eq. (13), for given constants* ε, μ_{lim}, $\varphi > 0$, *if symmetric positive definite matrix Q, output feedback gains* $\bar{K}_j$ *and positive scalars* γ, σ, ξ_1, ξ_2, ξ_3 *exist and such that* $(i,j = 1,2,3)$ *if and only if the following inequalities are true:*

$$\begin{bmatrix} \Gamma_{ij}^{11} & \Gamma_{ij}^{12} & 0 \\ * & \Gamma_{ij}^{22} & \Gamma_{ij}^{23} \\ * & * & -\xi_3^{-1}I \end{bmatrix} < 0 \tag{16}$$

$$\begin{bmatrix} -\left(\frac{\mu_{\lim}}{\varepsilon}\right)^2 I & \bar{K}_j \\ * & -\varphi^{-1}Q \end{bmatrix} < 0, \tag{17}$$

where

$$\begin{aligned} \Gamma_{ij}^{11} &= [A_{0i}Q]_s + \left[\frac{1+\varepsilon}{2}B_{20}\bar{K}_j\right]_\varepsilon + \xi_1^{-1}HH^{\mathrm{T}} \\ &\quad + \xi_2^{-1}HH^{\mathrm{T}} + \xi_3^{-1}HH^{\mathrm{T}}, \\ \Gamma_{ij}^{12} &= \left[B_{1i} \quad B_{20} \quad \frac{1-\varepsilon}{2}\bar{K}_j^{\mathrm{T}} \quad QC_1{}^{\mathrm{T}} \quad QE_{ai}^{\mathrm{T}} \quad \frac{1+\varepsilon}{2}\bar{K}_j^{\mathrm{T}}E_b^{\mathrm{T}}\right], \\ \Gamma_{ij}^{22} &= \mathrm{diag}\{-\gamma^2 I \quad -\sigma I \quad -\sigma^{-1}I \quad -I \quad -\xi_1^{-1}I \quad -\xi_2^{-1}I\}, \\ \Gamma_{ij}^{23} &= [0 \quad E_b \quad 0 \quad 0 \quad 0 \quad 0]^{\mathrm{T}} \end{aligned}$$

The robust H-infinity method is based on the principle that the robust H-infinity performance problem of the system is transformed into the solution problem of a linear matrix inequality system using Lyapunov stability theory. Therefore, Eqs. (16) and (17) are the necessary conditions for the computation of the output feedback gains in the LMIs designed in this paper.

Proof A Lyapunov function is chosen as follows:

$$V(t) = x^{\mathrm{T}}(t)Px(t), \tag{18}$$

where $P > 0$ is a symmetric matrix. The derivative of $V(t)$ is obtained as

$$\begin{aligned} \dot{V}(t) &= \dot{x}^T(t)Px(t) + x^T(t)P\dot{x}(t) \\ &= \sum_{i=1}^{3}\alpha_i\big[x^T(t)\big((A_{0i}+\Delta A_i)^TP + P(A_{0i}+\Delta A_i)\big)x(t) \\ &\quad + \omega^T(t)B_{1i}^TPx(t) + x^T(t)PB_{1i}\omega(t) \\ &\quad + \frac{1+\varepsilon}{2}x^T(t)P(B_{20}+\Delta B_2)u(t) \\ &\quad + \frac{1+\varepsilon}{2}u^T(t)(B_{20}+\Delta B_2)^TPx(t) \\ &\quad + \left(\bar{u}(t) - \frac{1+\varepsilon}{2}u(t)\right)^T(B_{20}+\Delta B_2)^TPx(t) \\ &\quad + x^T(t)P(B_{20}+\Delta B_2)\left(\bar{u}(t) - \frac{1+\varepsilon}{2}u(t)\right)\big] \end{aligned} \tag{19}$$

According to Eqs. (12), (19) can be expressed as

$$\begin{aligned} \dot{V}(t) &= \dot{x}^{\mathrm{T}}(t)Px(t) + x^{\mathrm{T}}(t)P\dot{x}(t) \\ &= \sum_{i=1}^{3}\sum_{j=1}^{3}\alpha_j\alpha_i\Big[x^{\mathrm{T}}(t)\Big((A_{0i}+\Delta A_i)^{\mathrm{T}}P \\ &\quad + P(A_{0i}+\Delta A_i)\Big)x(t) + \omega^{\mathrm{T}}(t)B_{1i}^{\mathrm{T}}Px(t) \\ &\quad + x^{\mathrm{T}}(t)PB_{1i}\omega(t) \\ &\quad + \frac{1+\varepsilon}{2}x^T(t)P(B_{20}+\Delta B_2)K_jC_yx(t) \\ &\quad + \frac{1+\varepsilon}{2}K_j^TC_y^{\mathrm{T}}(t)x^{\mathrm{T}}(t)(B_{20}+\Delta B_2)^{\mathrm{T}}Px(t) \\ &\quad + x^{\mathrm{T}}(t)P(B_{20}+\Delta B_2)\left(\bar{u}(t) - \frac{1+\varepsilon}{2}u(t)\right) \\ &\quad + \left(\bar{u}(t) - \frac{1+\varepsilon}{2}u(t)\right)^{\mathrm{T}}(B_{20}+\Delta B_2)^{\mathrm{T}}Px(t) \end{aligned} \tag{20}$$

According to Lemma 2, let $R = \left(u\bar{e}(t) - \frac{1+\varepsilon}{2}u(t)\right)^T$, $F = I$, and $S = (B_{20}+\Delta B_2)^TPx(t)$, then

$$\begin{aligned}\dot{V}(t) &= \dot{x}^{\mathrm{T}}(t)Px(t) + x^{\mathrm{T}}(t)P\dot{x}(t)\\ &= \sum_{i=1}^{3}\sum_{j=1}^{3}\alpha_j\alpha_i\Big[x^{\mathrm{T}}(t)\Big((A_{0i}+\Delta A_i)^{\mathrm{T}}P\\ &\quad +P(A_{0i}+\Delta A_i))x(t) + \omega^{\mathrm{T}}(t)B_{1i}^{T}Px(t)\\ &\quad + x^{\mathrm{T}}(t)PB_{1i}\omega(t)\\ &\quad + \frac{1+\varepsilon}{2}x^{\mathrm{T}}(t)P(B_{20}+\Delta B_2)K_jC_yx(t)\\ &\quad + \frac{1+\varepsilon}{2}K_j^{\mathrm{T}}C_y^{\mathrm{T}}(t)x^{\mathrm{T}}(t)(B_{20}+\Delta B_2)^{\mathrm{T}}Px(t)\\ &\quad + \sigma\left(\bar{u}(t)-\frac{1+\varepsilon}{2}u(t)\right)^{\mathrm{T}}\left(\bar{u}(t)-\frac{1+\varepsilon}{2}u(t)\right)\\ &\quad +\sigma^{-1}x^{\mathrm{T}}(t)P(B_{20}+\Delta B_2)(B_{20}+\Delta B_2)^{\mathrm{T}}Px(t)\Big]\end{aligned} \tag{21}$$

According to Lemma 1, we have

$$\begin{aligned}\dot{V}(t) &= \dot{x}^{\mathrm{T}}(t)Px(t) + x^{\mathrm{T}}(t)P\dot{x}(t)\\ &= \sum_{i=1}^{3}\sum_{j=1}^{3}\alpha_j\alpha_i\Big[x^{\mathrm{T}}(t)\Big((A_{0i}+\Delta A_i)^{\mathrm{T}}P\\ &\quad +P(A_{0i}+\Delta A_i))x(t) + \omega^{\mathrm{T}}(t)B_{1i}^{\mathrm{T}}Px(t)\\ &\quad + x^{\mathrm{T}}(t)PB_{1i}\omega(t)\\ &\quad + \frac{1+\varepsilon}{2}x^{\mathrm{T}}(t)P(B_{20}+\Delta B_2)K_jC_yx(t)\\ &\quad + \frac{1+\varepsilon}{2}K_j^{\mathrm{T}}C_y^{\mathrm{T}}(t)x^{\mathrm{T}}(t)(B_{20}+\Delta B_2)^{\mathrm{T}}Px(t)\\ &\quad + \sigma^{-1}x^{\mathrm{T}}(t)P(B_{20}+\Delta B_2)(B_{20}+\Delta B_2)^{\mathrm{T}}Px(t)\\ &\quad +\sigma\left(\frac{1-\varepsilon}{2}\right)^{2}u^{\mathrm{T}}(t)u(t)\Big]\end{aligned} \tag{22}$$

From Eq. (12), it can be shown that

$$\begin{aligned}\dot{V}(t) &= \dot{x}^{\mathrm{T}}(t)Px(t) + x^{\mathrm{T}}(t)P\dot{x}(t)\\ &= \sum_{i=1}^{3}\sum_{j=1}^{3}\alpha_i\alpha_j\Big[x^{\mathrm{T}}(t)\Big((A_{0i}+\Delta A_i)^{\mathrm{T}}P\\ &\quad + P(A_{0i}+\Delta A_i) + \frac{1+\varepsilon}{2}C_y^{\mathrm{T}}K_j^{T}(B_{20}+\Delta B_2)^{\mathrm{T}}P\\ &\quad + \frac{1+\varepsilon}{2}P(B_{20}+\Delta B_2)K_jC_y\\ &\quad + \sigma^{-1}P(B_{20}+\Delta B_2)(B_{20}+\Delta B_2)^{\mathrm{T}}P\\ &\quad +\sigma\left(\frac{1-\varepsilon}{2}\right)^{2}C_y^{\mathrm{T}}K_j^{\mathrm{T}}K_jC_y\Big)x(t)\\ &\quad +\omega^{\mathrm{T}}(t){B_{1i}}^{\mathrm{T}}Px(t) + x^{\mathrm{T}}(t)PB_{1i}\omega(t)\Big]\end{aligned} \tag{23}$$

Then, the following expression holds

$$\begin{aligned}J_{z\omega} &= \dot{V}(t) + z^{\mathrm{T}}(t)z(t) - \gamma^2\omega^{\mathrm{T}}(t)\omega(t)\\ &\le \mathrm{X}^{\mathrm{T}}(t)\left(\sum_{j=1}^{3}\sum_{i=1}^{3}\alpha_i\alpha_j\Lambda_{ij}\right)\mathrm{X}(t)\end{aligned} \tag{24}$$

where

$$\Lambda_{ij} = \begin{bmatrix}\Lambda_{ij1} & PB_{1i}\\ * & -\gamma^2 I\end{bmatrix}, \mathrm{X}(t) = \begin{bmatrix}x(t)\\ \omega(t)\end{bmatrix},$$

$$\begin{aligned}\Lambda_{ij1} &= [P(A_{0i}+\Delta A_i)]_s\\ &\quad + \frac{1+\varepsilon}{2}\left[P(B_{20}+\Delta B_2)K_jC_y\right]_s + C_1^{\mathrm{T}}C_1\\ &\quad + \sigma^{-1}P(B_{20}+\Delta B_2)(B_{20}+\Delta B_2)^{\mathrm{T}}P\\ &\quad + \sigma\left(\frac{1-\varepsilon}{2}\right)^{2}C_y^{\mathrm{T}}K_j^{\mathrm{T}}K_jC_y\end{aligned}$$

Using the Schur complement, it can be concluded that

$$\Lambda_{ij} = \begin{bmatrix}\zeta_1 & PB_{1i} & P(B_{20}+\Delta B_2) & \frac{1-\varepsilon}{2}{C_y}^{\mathrm{T}}{K_j}^{\mathrm{T}} & {C_1}^{\mathrm{T}}\\ * & -\gamma^2 I & 0 & 0 & 0\\ * & * & -\sigma I & 0 & 0\\ * & * & * & -\sigma^{-1}I & 0\\ * & * & * & * & -I\end{bmatrix}, \tag{25}$$

where $\zeta_1 = [P(A_{0i}+\Delta A_i)]_s + \frac{1+\varepsilon}{2}[P(B_{20}+\Delta B_2)K_jC_y]_s$.

Define $Q = P^{-1}$, $\bar{K}_j = K_jC_yQ$, and $J_1 = \mathrm{diag}\{Q\ I\ I\ I\ I\}$. Pre- and post-multiplying both sides of Eq. (25) with J_1, the matrix Λ_{ij} is equivalent to

$$\Phi_{ij} = \begin{bmatrix} \zeta_2 & B_{1i} & B_{20}+\Delta B_2 & \frac{1-\varepsilon}{2}\bar{K}_j^{\mathrm{T}} & QC_1^{\mathrm{T}} \\ * & -\gamma^2 I & 0 & 0 & 0 \\ * & * & -\sigma I & 0 & 0 \\ * & * & * & -\sigma^{-1}I & 0 \\ * & * & * & * & -I \end{bmatrix}, \tag{26}$$

where $\zeta_2 = [(A_{0i}+\Delta A_i)Q]_s + \left[\frac{1+\varepsilon}{2}(B_{20}+\Delta B_2)\bar{K}_j\right]_s$.

In light of Eq. (8), the following expressions hold

$$\begin{aligned} \Phi_{ij} = & \begin{bmatrix} \zeta_3 & B_{1i} & B_{20} & \frac{1-\varepsilon}{2}\bar{K}_j^{\mathrm{T}} & QC_1^{T} \\ * & -\gamma^2 I & 0 & 0 & 0 \\ * & * & -\sigma I & 0 & 0 \\ * & * & * & -\sigma^{-1}I & 0 \\ * & * & * & * & -I \end{bmatrix} \\ & + \left[\begin{bmatrix} H^{\mathrm{T}} & 0 & 0 & 0 & 0 \end{bmatrix}^{\mathrm{T}} \Gamma \begin{bmatrix} E_{ai}Q & 0 & 0 & 0 & 0 \end{bmatrix} \right]_s \\ & + \left[\frac{1+\varepsilon}{2} \begin{bmatrix} H^{\mathrm{T}} & 0 & 0 & 0 & 0 \end{bmatrix}^{\mathrm{T}} \Gamma \begin{bmatrix} E_{bi}\bar{K}_j & 0 & 0 & 0 & 0 \end{bmatrix} \right]_s \\ & + \left[\begin{bmatrix} H^{\mathrm{T}} & 0 & 0 & 0 & 0 \end{bmatrix}^{\mathrm{T}} \Gamma \begin{bmatrix} 0 & 0 & E_{bi} & 0 & 0 \end{bmatrix} \right]_s \end{aligned}, \tag{27}$$

where $\zeta_3 = [A_{0i}Q]_s + \left[\frac{1+\varepsilon}{2}B_{20}\bar{K}_j\right]_s$.

From Eq. (27), it can be shown that $\phi_{ij} < 0$ is equivalent to Eq. (16), then $\dot{V}(t) < 0$. The concerned vehicle system is asymptotically stable and the H_∞ performance criterion is satisfied. Symbol $[.]_s$ denotes the sum of its internal matrix and its transpose.

Moreover, under zero initial state, processing Eq. (24) by integrating the two sides from 0 to t, it can be concluded that

$V(t) = x^{\mathrm{T}}(t)Px(t) \le \gamma^2 \int_0^t \omega^{\mathrm{T}}(t)\omega(t)\mathrm{d}t \le \gamma^2\|\omega(t)\|_2^2 \le \gamma^2\varphi.$

Then, the following expressions hold:

$$\begin{aligned} \max_{t\ge 0} u(t)^2 &= \max_{t\ge 0} \left\| u^{\mathrm{T}}(t)u(t) \right\|_2 \\ &= \max_{t\ge 0} \left\| x^{\mathrm{T}}(t)C_y^{\mathrm{T}}K_j^{\mathrm{T}}K_jC_yx(t) \right\|_2 \\ &= \max_{t\ge 0} \left\| \bar{x}^{\mathrm{T}}(t)P^{-1/2}C_y^{\mathrm{T}}K_j^{\mathrm{T}}K_jC_yP^{-1/2}\bar{x}(t) \right\|_2 \\ &\le \varphi\lambda_{\max}\left(P^{-1/2}C_y^{\mathrm{T}}K_j^{\mathrm{T}}K_jC_yP^{-1/2} \right) \end{aligned}, \tag{28}$$

where $\lambda_{\max}(\cdot)$ denotes the maximum value of a matrix eigenvalue. Furthermore, the saturation constraint is satisfied when the following inequality is true.

$$P^{-1/2}C_y^{\mathrm{T}}K_j^{\mathrm{T}}K_jC_yP^{-1/2} \le \left(\frac{\mu_{\lim}}{\varepsilon}\right)^2 I \tag{29}$$

Employing the Schur complement, it can be concluded that

$$\begin{bmatrix} -\left(\frac{\mu_{\lim}}{\varepsilon}\right)^2 I & K_jC_yP^{-1/2} \\ * & -\varphi^{-1} \end{bmatrix} < 0. \tag{30}$$

Denote $J_2 = \mathrm{diag}\{I, P^{-1/2}\}$, when Eq. (30) is pre- and post-multiplied by J_2, Eq. (30) is equivalent to Eq. (17). The proof is now complete. □

Remark 2 Given that there are two unknown matrices K_j and Q in element $\bar{K}_j$, the conditions in Theorem are not convex anymore. So, calculating the output feedback gain matrix K_j directly by Theorem 1 is infeasible, and sufficient conditions will be presented in Theorem 2 for controller optimization and computation.

3.2 Controller Optimization and Computation

Theorem 2 *The concerned vehicle system in Eq. (10) is asymptotically stable and meets the desired performance in Eq. (13), for given constants* ε, μ_{lim}, $\varphi > 0$, *if symmetric positive definite matrix* X_W, X_R, *feedback gains* Y_{Rj} *and positive scalars* γ, σ, ξ_1, ξ_2, ξ_3 *exist and such that* $(i,j = 1,2,3)$.

$$\begin{bmatrix} \bar{\Gamma}_{ij}^{11} & \bar{\Gamma}_{ij}^{12} & 0 \\ * & \Gamma_{ij}^{22} & \Gamma_{ij}^{23} \\ * & * & -\xi_3^{-1}I \end{bmatrix} < 0 \tag{31}$$

$$\begin{bmatrix} -\left(\frac{\mu_{\lim}}{\varepsilon}\right)^2 I & Y_{Rj}R^{\mathrm{T}} \\ * & -\varphi^{-1}(WX_WW^T + RX_RR^{\mathrm{T}}) \end{bmatrix} < 0, \tag{32}$$

where

$$\begin{aligned} \bar{\Gamma}_{ij}^{11} &= \left[A_{0i}\left(WX_WW^T + RX_RR^T\right)\right]_s + \left[\frac{1+\varepsilon}{2}B_{20}\bar{K}_j\right]_s \\ &\quad + \xi_1^{-1}HH^T + \xi_2^{-1}HH^T + \xi_3^{-1}HH^T, \\ \bar{\Gamma}_{ij}^{12} &= \left[B_{1i}, B_{20}, \frac{1-\varepsilon}{2}\left(Y_{Rj}R^T\right)^T, \left(WX_WW^T + RX_RR^T\right)C_1^T, \right. \\ &\quad \left. \left(WX_WW^T + RX_RR^T\right)E_{ai}^T, \frac{1+\varepsilon}{2}\left(Y_{Rj}R^T\right)^T E_b^T \right] \end{aligned}$$

Then, the SOF control gains K_j is easy to calculate by $K_j = Y_{Rj}X_R^{-1}$.

Proof From [35], the matrices Q and $\bar{K}_j$ can be written as follows:

$$\begin{cases} Q = WX_W W^{\mathrm{T}} + RX_R R^{\mathrm{T}} \\ \bar{K}_j = Y_{Rj} R^{\mathrm{T}} \end{cases} \tag{33}$$

where W is a matrix satisfying $C_y W = 0$. R is defined as $R = C_y^{\dagger} + WM$, where M is a given matrix with suitable dimensions, and $C_y^{\dagger} = C_y^{\mathrm{T}} \left(C_y C_y^{\mathrm{T}} \right)^{-1}$.

Motivated by the above definition, $CR = I$ and $CQ = 0$ can be derived. Furthermore, the following equations hold:

$$C_y Q = C_y \left(WX_W W^{\mathrm{T}} + RX_R R^{\mathrm{T}} \right) = X_R R^T \tag{34}$$

$$\begin{aligned} &\bar{K}_j = Y_{Rj} R^{\mathrm{T}} = K_j C_y Q \\ \Leftrightarrow\ &K_j = Y_{Rj} R^{\mathrm{T}} \left(X_R R^{\mathrm{T}} \right)^{-1} = Y_{Rj} X_R^{-1} \end{aligned} \tag{35}$$

Hence, the desired output feedback gain K_j can be acquired. □

Remark 3 The H-infinity output feedback control algorithm is employed to design the controller, and the actuator saturation is also considered in the controller design, which not only reduces the measurement cost and maintains the feasibility of the controller, but also enhances the control effect and maximizes the overall performance of the system.

4 Experiment

In this part, in order to evaluate the feasibility of the proposed controller, two typical maneuvers, comprising a single-lane change maneuver and a J-turn maneuver, are executed on hardware-in-the-loop (HIL) experimental platform bases on the LabVIEW RT system. Figure 3 depicts the HIL experimental platform. The experiment platform consists of a G29 simulator, cRIO, PXI, host computer, etc. The vehicle model and road information in CarSim are embedded into PXI RT system, and the control algorithm is embedded into LabVIEW RT system by compiling of MATLAB. The steering angle, which is calculated by cRIO, acts on the G29 driving simulator. The communication between components is performed through CAN signals.

Since Carsim includes modeling functions for road scenarios and working conditions, different road environments can be established. A variety of scenarios and working conditions can be designed to meet the development and verification of the control system under different environments. Therefore, the experimental tests can be implemented by selecting corresponding vehicle model and parameters, and then the effectiveness of the designed controller can be verified by performing vehicle path tracking performance analysis on the selected road.

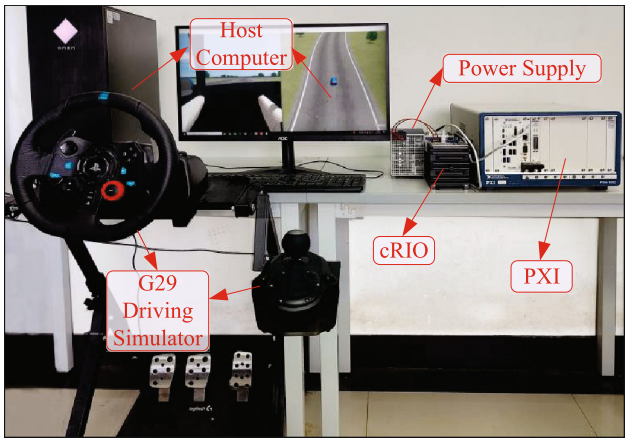

Fig. 3 Physical diagram of the HIL experimental test

Figure 4 shows the structure diagram of the HIL experimental test. Table 1 lists the parameter values of the FWID-EVs used in this experiment. Considering that the parameters m, I_z, C_f , and C_r are nonlinear and time-varying in real practice, the nominal values of these parameters are provided first, as listed in Table 1. Specially, v_x is set as 20 m/s initially but varies within the upper and lower limits. The uncertainty of cornering stiffness is regarded as 20% of the nominal value for both the front and rear wheels, whereas the moment of inertia and vehicle mass are regarded as 20% variances. Among them, the upper and lower speed limits are also given together in the table. Moreover, the saturation bounds of steering angle and external yaw moment are defined as $25deg$ and 3000 N, respectively (i.e., $\mu_{lim} = [25 \quad 3000]^{\mathrm{T}}$). Besides, $\varphi = 0.02$ and $\varepsilon = 0.95$ are chosen. The external disturbances are chosen as $d_1 = 0.001$ m/s^2, $d_2 = 0.002$ rad/s^2 and $d_3 = 0.003$ m/s. Then, Controller A is the name of the RHF-SOF controller proposed in this research, and the controller gain matrix is determined as

$$K_{\mathrm{sof}} = \begin{bmatrix} -1.05 & -23.84 & -0.74 \\ -119466 & -1610969 & -47660 \end{bmatrix}.$$

To emphasize the advantage of Controller A presented in this research, the output feedback controller (i.e., Controller B) with input saturation presented in [36] is adopted as a comparative counterpart. The SOF gains can be acquired as

$$K_B = \begin{bmatrix} -7.64 & -74.60 & -4.76 \\ -22354 & -60880 & -1029 \end{bmatrix}.$$

4.1 Example: 1

The single-lane change maneuver is to operate the vehicle through a single-lane change to follow the target lane, and therefore reflects vehicle tracking accuracy and handling

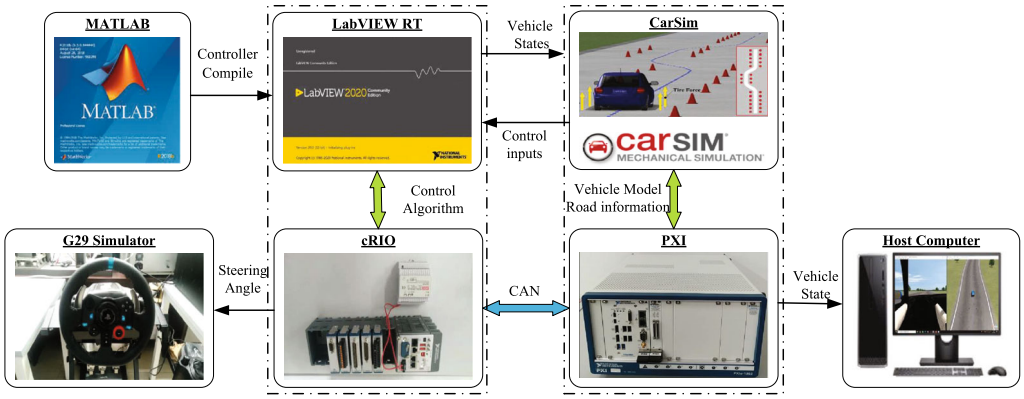

Fig. 4 Structure diagram of the HIL experimental test

Table 1 Model parameter values of FWID-EVs

Parameters	Value	Unit	Parameters	Value	Unit
m	1412	kg	C_f	49412	N/rad
I_z	1536.7	kg m^2	C_r	60174	N/rad
l_f	1.059	m	$v_{x\max}$	30	m/s
l_r	1.641	m	$v_{x\min}$	10	m/s
v_x	20	m/s	–	–	–

stability. As shown in Fig. 5 a, the response of FWID-EVs under the single-lane change maneuver is demonstrated. The longitudinal velocity is described in Fig. 5b. It is noteworthy that the longitudinal velocity of FWID-EVs is accelerated at first and decelerated later.

The system performance indexes and performance comparisons of FWID-EVs under the control of different controllers can be acquired, which is shown in Fig. 6a, c, and d exhibit that Controller A can obviously decrease the lateral velocity, lateral offset, and heading error to achieve dynamic stability faster as compared with Controller B. Figure 6b shows that the yaw rate produced in both the control strategies are close. In terms of preserving the vehicle's handling stability, the path-following performance of Controller A is superior to that of Controller B, as shown in Fig. 6.

Table 2 presents the root mean square (RMS) values of system performance for various controllers for additional quantitative investigation. Although the lateral velocity and yaw rate show minor improvement, as compared to Controller B, the lateral offset and heading error of Controller A are reduced by 9.81% and 40.22%, respectively. It can be concluded that the proposed controller can maintain more accurate tracking performance and simultaneously improve the handling stability of the vehicle during lane changing maneuver.

Figure 7 depicts the input situation of actuators with different control strategies. It can be found that the saturation conditions of actuators in all control strategies are bounded in the given limits.

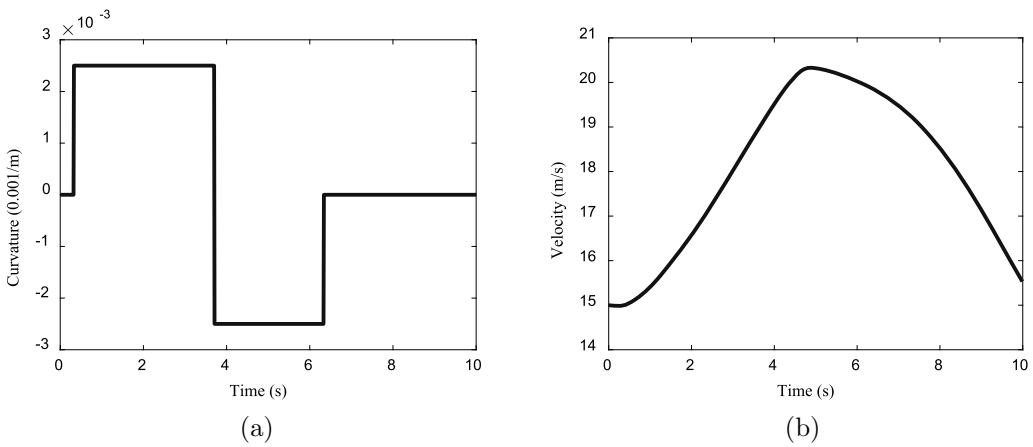

Fig. 5 Example 1: **a** road curvature, **b** longitudinal velocity

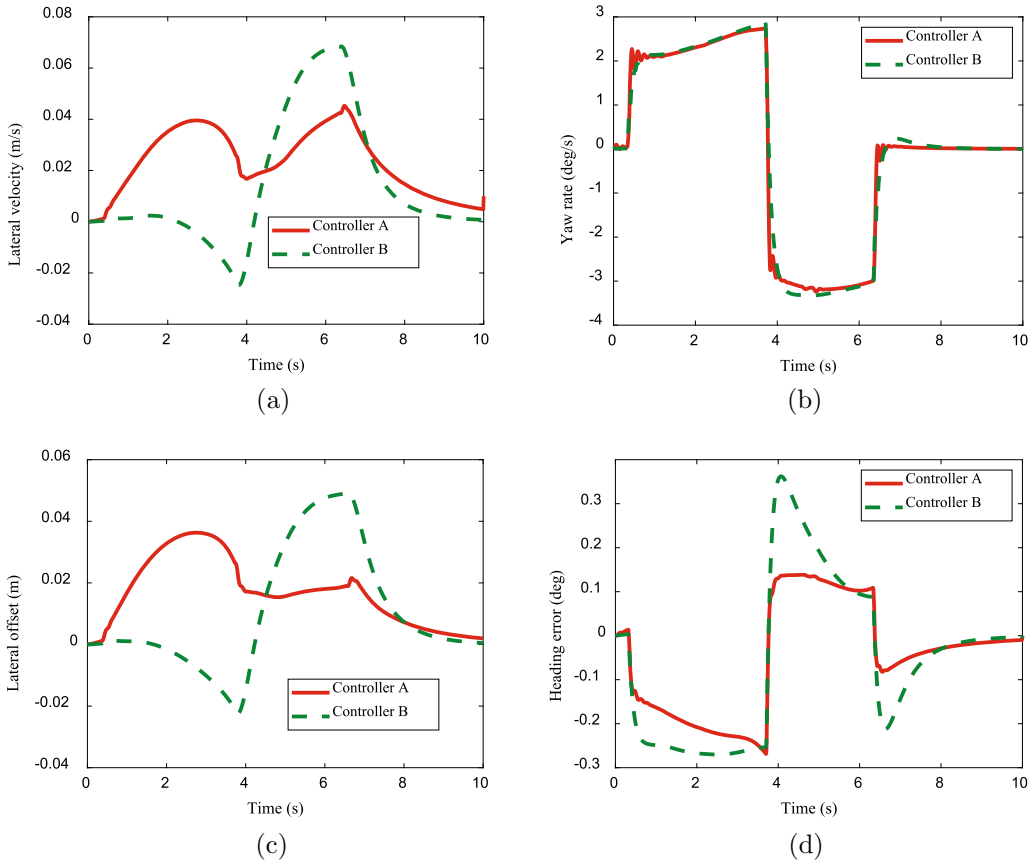

Fig. 6 Example 1: **a** lateral velocity, **b** yaw rate, **c** lateral offset, **d** heading error

Table 2 RMS values of path-following errors in Example 1

Index	v_y	r	ψ	e
Controller B	1.1557	2.1120	0.1914	0.0291
Controller A	1.1421 (− 1.19%)	2.0831 (− 1.39%)	0.1365 (− 40.22%)	0
				0.0265 (− 9.81%)

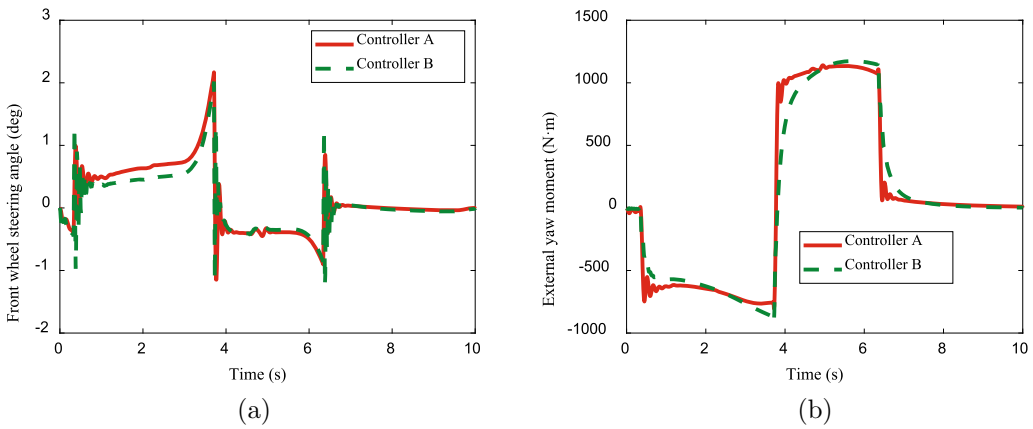

Fig. 7 Example 1: **a** front wheel steering input, **b** external yaw moment

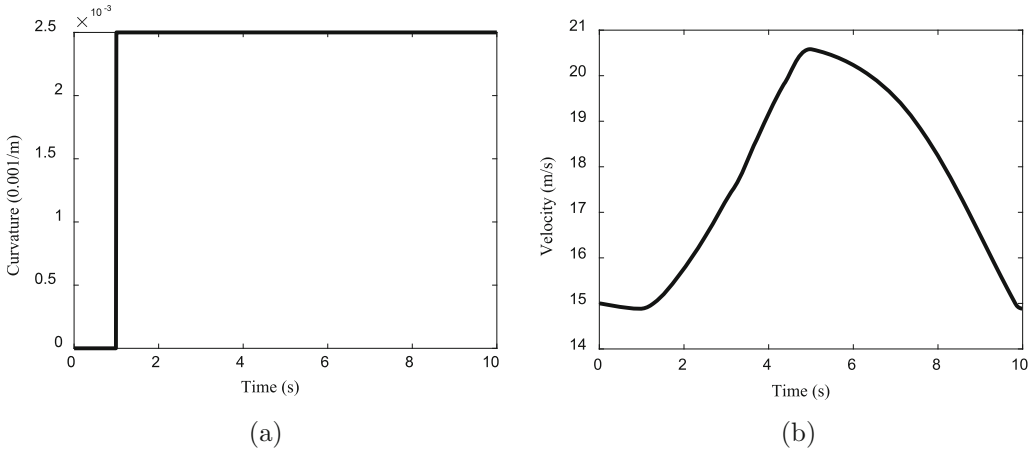

Fig. 8 Example 2: (a) road curvature, (b) longitudinal velocity

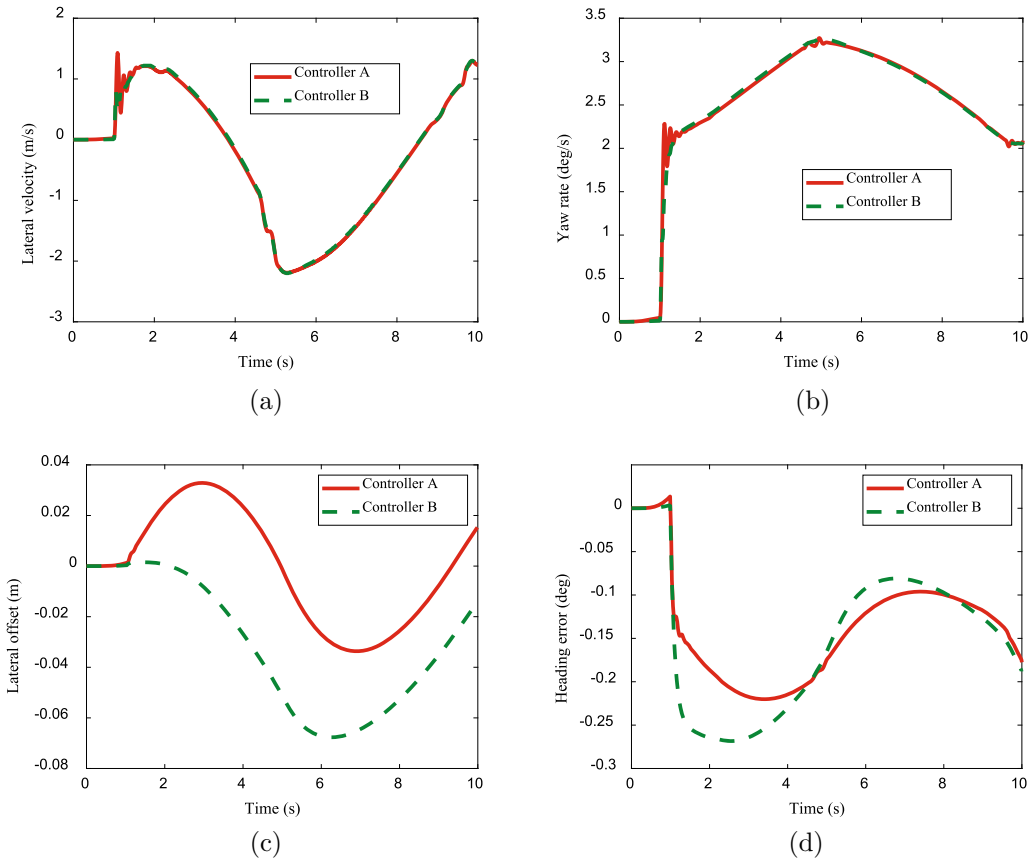

Fig. 9 Example 2: **a** lateral velocity, **b** yaw rate, **c** lateral offset, **d** heading error

Table 3 RMS values of path-following errors in Example 2

Index	v_y	r	ψ	e
Controller B	1.1291	2.5718	0.1723	0.0403
Controller A	0.1137 (− 1.38%)	2.45 (− 0.11%)	0.1685 (− 14.03%)	0.0188 (− 82.35%)

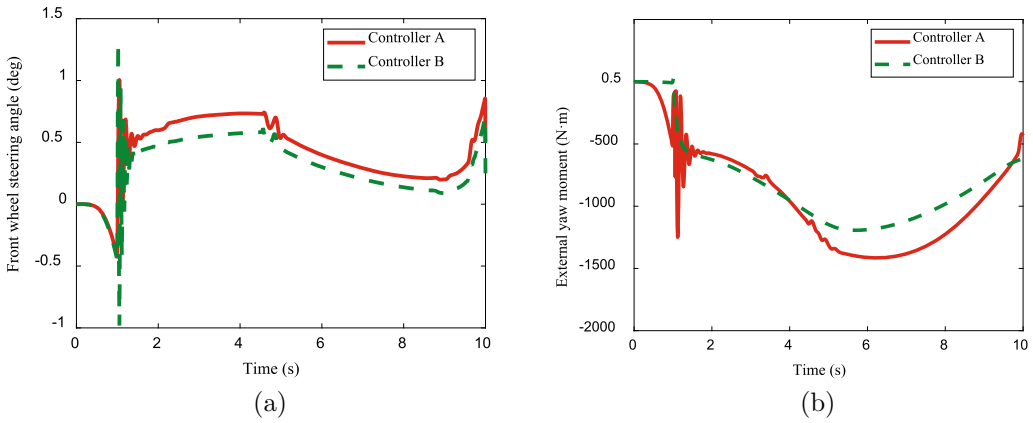

Fig. 10 Example 2: (a) front wheel steering input, (b) external yaw moment

4.2 Example: 2

The J-turn maneuver is produced from the ramp steering input, and this maneuver is used to examine the cornering stability under extreme steering conditions. Therefore, the dynamic response of the vehicle during a J-turn maneuver is studied. Figure 8 shows the longitudinal velocity and road curvature change.

Figure 9 illustrates the system performance indexes for the J-turn maneuver. As demonstrated in Fig. 9, despite the fact that the lateral velocity and yaw rate of Controller A have a slight performance improvement Controller B, lateral offset and heading error exhibit notable enhancements. This demonstrates that the path-following performance is greatly improved with the proposed control strategy. The RMS values of system performance indexes in Example 2 are listed in Table 3, which shows that Controller A can reduce the heading error and the lateral offset by 14.03% and 82.35%, respectively, as compared with Controller B.

In J-turn maneuver, the longitudinal speed is lower than that in the single-lane change maneuver, but the road curvature is higher, and the actuator saturation is more likely to happen. Figure 10 shows the outcomes of the front wheel steering and the external yaw moment. The external yaw moment is far from $\pm$ 3000 N and both controllers are able to operate the actuator within a reasonable range. It shows that the designed controller is effective in avoiding actuator saturation even under extreme conditions (i.e., high curvature road conditions).

Remark 4 The objective of this work is to enhance the path-following performance of the vehicle while ensuring actuator saturation. From the point of view of the control signal, a higher execution action amplitude can be obtained from the proposed strategy and thus better performance can be guaranteed with satisfied saturation condition. This benefits from the valid sufficient condition in Theorem 2.

5 Conclusion

In this research, a RHF-SOF control strategy was designed to improve the path-following performance for nonlinear FWID-EVs with actuator saturation.

According to experimental results, the proposed controller shows advantages in achieving path-following performance. The following conclusions can be drawn:

(1) The proposed simulation result shows that the vehicle performance with the proposed RHF-SOF control approach is superior to output feedback control approach in [36]. This implies that the proposed controller has better robustness and can solve the problem of parameter uncertainty and nonlinearity;
(2) The fuzzy optimization model integrates LFT and gain scheduling, which greatly helps to achieve parameter estimation, including vehicle longitudinal speed, vehicle mass, moment of inertia, longitudinal speed, and tire turning stiffness. This means that a more accurate vehicle model can be deployed to the vehicle controller;
(3) The norm-bounded strategy is effective for vehicle nonlinear actuator saturation problems. This prevents unstable, fluctuations and other factors that can seriously affect controller performance.

Considering that the model is built based on active steering in this paper, more effort will be devoted to the investigation of the controller design for human–machine cooperative driving in the future work.

Acknowledgements This work is supported by National Natural Science Foundation of China (Grant No. 52175127), the Natural Science Foundation of Guangdong Province of China (Grant No. 2022A1515011495), the China Postdoctoral Science Foundation (Grant No. 2022M712383), the Joint Project of Natural Science Foundation of Liaoning Province of China (Grant No. 2021-KF-11-02), the Fundamental Research Funds for the Central Universities

(Grant No. N2203012), and the research Grant of the University of Macau (Grant Nos. MYRG2020-00045-FST and MYRG2022-00099-FST).

References

1. Li, Z., Khajepour, A., Song, J.: A comprehensive review of the key technologies for pure electric vehicles. Energy **182**, 824–839 (2019)
2. Zhang, C., Yang, F., Ke, X., Liu, Z., Yuan, C.: Predictive modeling of energy consumption and greenhouse gas emissions from autonomous electric vehicle operations. Appl. Energy **254**, 113597 (2019)
3. Zhou, H., Liu, Z., Yang, X.: Motor torque fault diagnosis for four wheel independent motor-drive vehicle based on unscented Kalman filter. IEEE Trans. Veh. Technol. **67**(3), 1969–1976 (2018)
4. Liang, Y., Li, Y., Khajepour, A., Zheng, L.: Multi-model adaptive predictive control for path following of autonomous vehicles. IET Intell. Transp. Syst. **14**(14), 2092–2101 (2021)
5. Zhao, J., Li, W., Hu, C., Guo, G., Xie, Z., Wong, P.K.: Robust gain-scheduling path following control of autonomous vehicles considering stochastic network-induced delay. IEEE Trans. Intell. Transp. Syst. **23**(12), 23324–23333 (2022)
6. Sonker, R., Dutta, A.: Adding terrain height to improve model learning for path tracking on uneven terrain by a four wheel robot. IEEE Robot. Autom. Lett. **6**(1), 239–246 (2021)
7. Liang, Y., Li, Y., Khajepour, A., Zheng, L.: Holistic adaptive multi-model predictive control for the path following of 4wid autonomous vehicles. IEEE Trans. Veh. Technol. **70**(1), 69–81 (2021)
8. Taghavifar, H., Hu, C., Qin, Y., Wei, C.: Ekf-neural network observer based type-2 fuzzy control of autonomous vehicles. IEEE Trans. Intell. Transp. Syst. **22**(8), 4788–4800 (2021)
9. Zhao, J., Xiao, Y., Liang, Z., Wong, P.K., Xie, Z., Ma, X.: Adaptive event-triggered interval type-2 t-s fuzzy control for lateral dynamic stabilization of aevs with intermittent measurements and actuator failure. IEEE Trans. Transp. Electrific. (2022). https://doi.org/10.1109/TTE.2022.3204354
10. Ma, X., Wong, P.K., Zhao, J., Xie, Z.: Cornering stability control for vehicles with active front steering system using t-s fuzzy based sliding mode control strategy. Mech. Syst. Signal Proc. **125**, 347–364 (2019)
11. Chen, L., Li, P., Lin, W., Zhou, Q.: Observer-based fuzzy control for four-wheel independently driven electric vehicles with active steering systems. Int. J. Fuzzy Syst. **22**(1), 89–100 (2019)
12. Ren, H., Chen, L., Zhou, Q.: Fuzzy control for uncertain electric vehicle systems with sensor failures and actuator saturation. Int. J. Fuzzy Syst. **22**(5), 1444–1453 (2020)
13. Hu, C., Jing, H., Wang, R., Yan, F., Chadli, M.: Robust H_∞ output-feedback control for path following of autonomous ground vehicles. Mech. Syst. Signal Proc. **70–71**, 414–427 (2016)
14. Hang, P., Xia, X., Chen, X.: Handling stability advancement with 4ws and dyc coordinated control: a gain-scheduled robust control approach. IEEE Trans. Veh. Technol. **70**(4), 3164–3174 (2021)
15. Chu, S., Xie, Z., Wong, P.K., Li, P., Li, W., Zhao, J.: Observer-based gain scheduling path following control for autonomous electric vehicles subject to time delay. Veh. Syst. Dyn. **60**(5), 1602–1626 (2022)
16. Setiawan, Y.D., Nguyen, T.H., Pratama, P.S., Kim, H.K., Kim, S.B.: Path tracking controller design of four wheel independent steering automatic guided vehicle. Int. J. Control Autom. Syst. **14**(6), 1550–1560 (2016)
17. Li, B., Du, H., Li, W., Zhang, B.: Dynamically integrated spatiotemporal-based trajectory planning and control for autonomous vehicles. IET Intell. Transp. Syst. **12**(10), 1271–1282 (2018)
18. Guo, J., Wang, J., Luo, Y., Li, K.: Takagi-sugeno fuzzy-based robust h-infinity integrated lane-keeping and direct yaw moment controller of unmanned electric vehicles. IEEE-ASME Trans. Mechatron. **26**(4), 2151–2162 (2021)
19. Chang, Y., Sun, T., Zhang, X., Chen, X.: Output feedback stabilization for a class of cascade nonlinear ode-pde systems. Int. J. Control Autom. Syst. **19**(7), 2519–2528 (2021)
20. Zhang, Z.H., Li, S., Yan, H.: Interval observer-based output feedback control for a class of interconnected systems with uncertain interconnections. Int. J. Control Autom. Syst. **17**(4), 957–965 (2019)
21. Cong, L., Hui, J., Wang, R., Nan, C.: Vehicle lateral motion regulation under unreliable communication links based on robust H_∞ output-feedback control schema. Mech. Syst. Signal Proc. **104**, 171–187 (2018)
22. Viadero-Monasterio, F., Boada, B.L., Boada, M.J.L., Díaz, V.: H_∞ dynamic output feedback control for a networked control active suspension system under actuator faults. Mech. Syst. Signal Proc. **162**, 108050 (2022)
23. Li, Z.M., Chang, X.H., Park, J.H.: Quantized static output feedback fuzzy tracking control for discrete-time nonlinear networked systems with asynchronous event-triggered constraints. IEEE Trans. Syst. Man Cybern. B **51**(6), 3820–3831 (2021)
24. Chang, X.H., Yang, G.H.: Nonfragile H_∞ Filter Design for T-S Fuzzy Systems in Standard Form. IEEE Trans. Ind. Electron. **61**(7), 3448–3458 (2014)
25. Zhao, J., Wang, X., Wong, P.K., Xie, Z., Jia, J., Li, W.: Multi-objective frequency domain-constrained static output feedback control for delayed active suspension systems with wheelbase preview information. Nonlinear Dyn. **103**(2), 1757–1774 (2021)
26. Ouyang, D., Shao, J., Jiang, H., Nguang, S.K., Shen, H.T.: Impulsive synchronization of coupled delayed neural networks with actuator saturation and its application to image encryption. Neural Netw. **128**, 158–171 (2020)
27. Yan, M., Tang, Y., Yang, P., Zuo, L.: Consensus based platoon algorithm for velocity-measurement-absent vehicles with actuator saturation. J. Adv. Transp. **2017**, 8023018 (2017)
28. Xu, L., Yu, Y., Cui, Y.: Acceleration feedback active vibration control for seismic excited building structures with actuator saturation. Soil Dyn. Earthq. Eng. **115**, 472–475 (2018)
29. Yang, H., Jiang, B., Yang, H., Liu, H.H.T.: Synchronization of multiple 3-dof helicopters under actuator faults and saturations with prescribed performance. ISA Trans. **75**, 118–126 (2018)
30. Zhang, Z., Song, R., Cao, M.: Synchronous optimal control method for nonlinear systems with saturating actuators and unknown dynamics using off-policy integral reinforcement learning. Neurocomputing **356**, 162–169 (2019)
31. Zhao, J., Wang, X., Liang, Z., Li, W., Wang, X., Wong, P.K.: Adaptive event-based robust passive fault tolerant control for nonlinear lateral stability of autonomous electric vehicles with asynchronous constraints. ISA Trans. **127**, 310–323 (2022)
32. Zhang, H., Zhang, X., Wang, J.: Robust gain-scheduling energy-to-peak control of vehicle lateral dynamics stabilisation. Veh. Syst. Dyn. **52**(3), 309–340 (2014)
33. Du, H., Zhang, N., Naghdy, F.: Velocity-dependent robust control for improving vehicle lateral dynamics. Transp. Res. Pt. C **19**(3), 454–468 (2011)
34. Du, H., Zhang, N.: Fuzzy control for nonlinear uncertain electrohydraulic active suspensions with input constraint. IEEE Trans. Fuzzy Syst. **17**(2), 343–356 (2009)
35. Rubio-Massegu, J., Rossell, J.M., Karimi, H.R., Palacios-Quinonero, F.: Static output-feedback control under information structure constraints. Automatica **49**(1), 313–316 (2013)

36. Li, P., Li, P., Zhao, J., Zhang, B.: Robust gain-scheduling static output-feedback H_∞ control of vehicle lateral stability with heuristic approach. Inf. Sci. **546**, 220–233 (2021)

Taiyou Liu has received his M.S. degree in Electromechanical Engineering from the University of Macau, Macao, China, in 2019. He is currently working toward his Ph.D. degree in Mechanical Engineering from the School of Mechanical Engineering and Automation, Northeastern University, Shenyang, China. His research interests include vehicle dynamics and control of autonomous four-wheel-independent-drive vehicles.

Xiaowei Wang has received his M.S. degree in Mechanical Engineering from Northeastern University, Shenyang, China, in 2022. He is currently working toward his Ph.D. degree in Mechanical Engineering from the School of Mechanical Engineering and Automation, Northeastern University, Shenyang, China. His research interests include vehicle system dynamics and control.

Jing Zhao has received his Ph.D. degree in Electromechanical Engineering from University of Macau, Macao, China, in 2016. He is currently working with the School of Mechanical Engineering and Automation, Northeastern University. His research interests include vehicle dynamics and control, mechanism and machine theory, fluid mechanics, and finite element analysis.

Pak Kin Wong has received his Ph.D. degree in Mechanical Engineering from The Hong Kong Polytechnic University, Hong Kong, in 1997. He is currently a Professor in the Department of Electromechanical Engineering and Interim Dean of Graduate School, University of Macau. His research interests include automotive engineering, fluid transmission & control, mechanical vibration, and medical engineering. He has published over 284 scientific papers in refereed journals, book chapters, and conference proceedings. 166 out of 284 are SCI-E journal papers.

Yongfu Wang has received his Ph.D. degree in Control Science and Engineering from Northeastern University, Shenyang, China, in 2005. He is currently a Professor with the School of Mechanical Engineering and Automation, Northeastern University, Shenyang, China. His research interests include unmanned vehicles, intelligent modeling, and control of mechatronic systems.